Hexapartite coherent feedback control in four-wave mixing with a spatially structured pump

Haiyan He,[1] Kai Zhang,[1,5,*] and Jietai Jing[1,2,3,4,†]

[1]*State Key Laboratory of Precision Spectroscopy, Joint Institute of Advanced Science and Technology, School of Physics and Electronic Science, East China Normal University, Shanghai 200062, China*

[2]*CAS Center for Excellence in Ultra-Intense Laser Science, Shanghai 201800, China*

[3]*Collaborative Innovation Center of Extreme Optics, Shanxi University, Taiyuan, Shanxi 030006, China*

[4]*National Laboratory of Solid State Microstructures, Nanjing University, Nanjing 210093, China*

[5]*Chongqing Key Laboratory of Precision Optics, Chongqing Institute of East China Normal University, Chongqing 401120, China*

(Received 4 December 2023; accepted 16 May 2024; published 7 June 2024)

Quantum coherent feedback control (CFC) has been widely applied to prepare and manipulate nonclassical beams. In this paper, we utilize an optical beam splitter with tunable reflectivity k as a feedback controller and theoretically construct a CFC system based on four-wave mixing (FWM) processes with a spatially structured pump. After considering absorption loss in the atoms, beam propagation loss in the feedback loop, and detection loss in the detectors, we derive an input-output relationship and theoretically study the manipulation of feedback strength, gain of the FWM processes, and phase to the degree of hexapartite quantum correlation of the system. We find that the relative intensity-difference squeezing degree of all the six output fields from this system is enhanced within a certain range of feedback ratio and phase. Furthermore, there exists an optimal feedback ratio and phase to maximize the intensity-difference squeezing. In addition, we also study the entanglement properties of this CFC system by the positivity under the partial transposition criterion and find that the feedback ratio and phase can tailor the entanglement structure of the hexapartite state. The proposed CFC scheme has realized quantum correlation enhancement and entanglement manipulation, which can be expanded to a large-scale quantum network for more practical applications in quantum information processing.

DOI: 10.1103/PhysRevA.109.062409

I. INTRODUCTION

Quantum control theory plays a fundamental role in emerging quantum technology [1,2], which has been widely studied and applied in quantum information processing [3]. In a quantum control field, feedback control [4] is an important control method, which is divided into two main classes. Coherent feedback control (CFC) [5,6] is different from measurement-based feedback control [7,8]. The former non-measurement-based protocol has been extensively used in quantum systems [9] to effectively manipulate the quantum system by feeding the output signal back to the original input, driving the entirety towards a desired state. For instance, the CFC has been utilized to prepare and manipulate nonclassical beams [10–13]. The coherence of the system will be maintained without destroying its quantum properties since the quantum CFC process is measurement free and does not introduce additional measurement noise [14,15]. Accordingly, quantum CFC has been employed in quantum error correction [16,17], enhancement of quantum squeezing [10,11,18], and entanglement [19].

Quantum correlation and entanglement are important resources in quantum information processing [20,21]. For this reason, it is vital to manipulate and even enhance the quantum correlation and entanglement [22]. CFC has been shown as a promising method to effectively enhance quantum correlation of twin beams generated by a single four-wave mixing (FWM) process [23]. The feedback strategy is also theoretically utilized in cascaded FWM processes [24], and it is proved that such quantum CFC system can enhance tripartite quantum correlation. In recent years, our group has experimentally [25,26] demonstrated reconfigurable hexapartite entanglement via FWM processes with a spatially structured pump (SSP) and theoretically [27] investigated its entanglement properties using the van Loock–Furusawa criterion [28] as well as the positivity under the partial transposition (PPT) criterion [29–31]. Moreover, the Einstein-Podolsky-Rosen steering characteristics of the hexapartite state [32] and the ability to generate reconfigurable cluster states [33] have been demonstrated. Different from prior works, in this paper, we introduce the CFC system to enhance the intensity-difference squeezing (IDS) and manipulate the entanglement of the SSP-based FWM system, which has important applications in the field of quantum information processing. Such a CFC system can also be easily extended to other multipartite states.

This paper is organized as follows. In Sec. II, we briefly describe the theoretical quantum CFC structure based on SSP-based FWM processes, and then derive the equations for the input and output beams produced by this CFC system after taking three kinds of losses, i.e., absorption loss in the atoms,

*Contact author: kzhang@lps.ecnu.edu.cn
†Contact author: jtjing@phy.ecnu.edu.cn

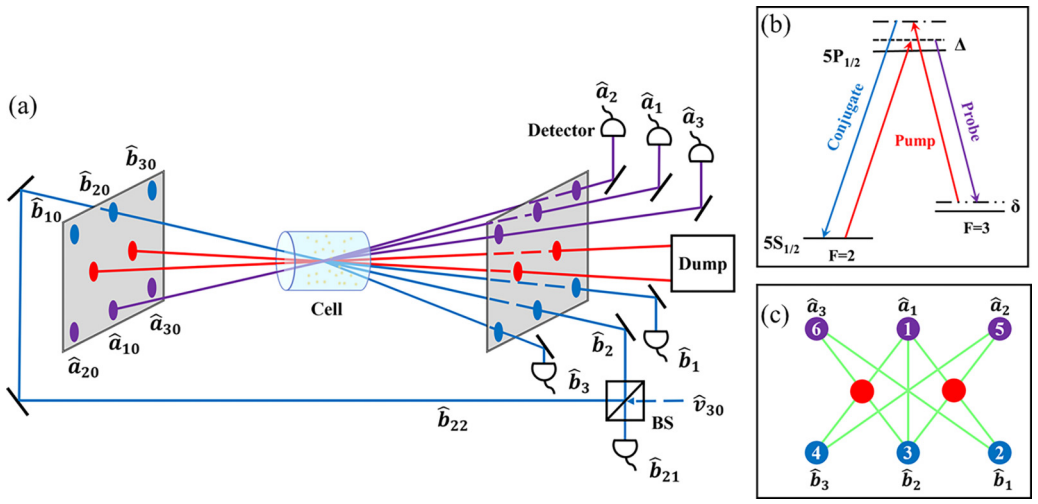

FIG. 1. The conceptional model of hexapartite CFC structure based on FWM processes with a SSP. (a) The two lines in the middle are pump beams. Cell is the hot ^{85}Rb atomic vapor cell with a length of 12 mm. $\hat{a}_{10}$ is the input probe beam. $\hat{b}_{10}$, $\hat{b}_{30}$, $\hat{a}_{20}$, $\hat{a}_{30}$, and $\hat{v}_{30}$ are vacuum inputs. $\hat{a}_1$ is the amplified probe beam. $\hat{a}_2$ and $\hat{a}_3$ are generated probe beams. $\hat{b}_1$, $\hat{b}_2$, and $\hat{b}_3$ are generated conjugate beams. (b) Involved double-Λ energy-level diagram for the D_1 line of ^{85}Rb. Δ refers to one-photon detuning of the pump from the transition $|5S_{1/2}, F = 2\rangle \rightarrow |5P_{1/2}\rangle$ and δ means two-photon detuning. (c) The spatial location distribution and the interaction structure of the six output beams from the SSP-based FWM processes. The dots in the first, second, and third rows stand for the probe beams, pump beams, and conjugate beams, respectively.

beam propagation loss in the feedback loop, and detection loss in the detectors, into consideration. In Sec. III, we investigate how the parameters, i.e., feedback ratio, phase induced by feedback loop, and interaction time, manipulate and even enhance the quantum correlation characterized by IDS between the six output fields. In Sec. IV, the manipulation to entanglement characterized by the symplectic eigenvalues is analyzed by tailoring the feedback ratio and phase. Finally, we summarize briefly the results in Sec. V.

II. FEEDBACK CONTROL STRUCTURE

The theoretical model of the hexapartite CFC configuration is illustrated in Fig. 1. As shown in Fig. 1(a), there are two identical strong pumps (lines in the middle) intersecting at the center of the hot ^{85}Rb atomic vapor cell with an angle of 8 mrad, each of which simultaneously converges with the coherent weak probe beam ($\hat{a}_{10}$). The angle between the probe beam and the plane of the two pump beams is approximately 5.7 mrad. To highlight optical spatial position, we draw a rectangle shaded area. In the SSP-based FWM processes, the original probe beam is amplified ($\hat{a}_1$). Two new probe beams ($\hat{a}_2$ and $\hat{a}_3$) and three conjugate beams ($\hat{b}_1$, $\hat{b}_2$, and $\hat{b}_3$) are generated synchronously [26]. Figure 1(b) depicts the double-Λ energy-level diagram for the D_1 line of ^{85}Rb in a single nonlinear FWM process, in which two pump photons annihilate, and one probe photon and one conjugate photon are produced at the same time. The spatial location layout and the nonlinear interaction framework of the six naturally separated output beams from the system can be seen from Fig. 1(c) in which the dots in the first, second, and third rows represent the probe, pump, and conjugate beams, respectively. The links with pump refer to single-pump FWM interactions, and those without pump mean dual-pump FWM interactions.

The SSP-based FWM processes contain seven interactions, i.e., four single-pump FWM interactions and three dual-pump FWM interactions. The Hamiltonian of such processes can be expressed as

$$\begin{aligned}\hat{H} = i\hbar[&\varepsilon_1\hat{a}_1^\dagger\hat{b}_1^\dagger + \varepsilon_2\hat{a}_1^\dagger\hat{b}_2^\dagger + \varepsilon_3\hat{a}_1^\dagger\hat{b}_3^\dagger + \varepsilon_4\hat{b}_2^\dagger\hat{a}_2^\dagger \\ &+ \varepsilon_5\hat{b}_2^\dagger\hat{a}_3^\dagger + \varepsilon_6\hat{b}_3^\dagger\hat{a}_2^\dagger + \varepsilon_7\hat{b}_1^\dagger\hat{a}_3^\dagger] + \text{H.c.},\end{aligned} \tag{1}$$

where ε_i ($i = 1, 2, 3, 4, 5, 6$, and 7) describes the effective interaction strength of the SSP-based FWM processes that is up to the pump power, one-photon and two-photon detuning. $\hat{a}_i^\dagger$ and $\hat{b}_i^\dagger$ ($i = 1, 2, 3$) denote the bosonic creation operators of output probe and conjugate beams, respectively. The two-dimensional intensity pattern of the output fields has been captured by camera in Ref. [26], from which it can be seen that the intensity of $\hat{a}_1$ and $\hat{b}_2$ is relatively strong, indicating a stronger interaction between them. Therefore, we set the interaction of ε_2 to be strongest. Owing to the balanced power and symmetrical structure of the two pump beams, we assume that $\varepsilon_1 = \varepsilon_3 = \varepsilon_4 = \varepsilon_5$ for four single-pump FWM interactions, and $\varepsilon_6 = \varepsilon_7$ for dual-pump FWM interactions between $\hat{b}_3$ and $\hat{a}_2$, as well as between $\hat{b}_1$ and $\hat{a}_3$, respectively. The interaction time is denoted as t. Solving Eq. (1), according to the Heisenberg equation of motion, the input-output relationship of the processes can be written as

$$\begin{pmatrix}\hat{a}_1\\ \hat{b}_1^\dagger\\ \hat{b}_2^\dagger\\ \hat{b}_3^\dagger\\ \hat{a}_2\\ \hat{a}_3\end{pmatrix} = A\begin{pmatrix}\hat{a}_{10}\\ \hat{b}_{10}^\dagger\\ \hat{b}_{20}^\dagger\\ \hat{b}_{30}^\dagger\\ \hat{a}_{20}\\ \hat{a}_{30}\end{pmatrix}, \tag{2}$$

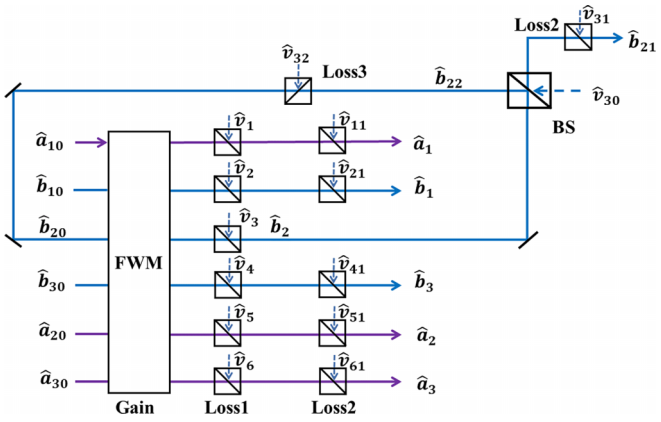

FIG. 2. The conceptional gain and loss model of hexapartite CFC structure on the basis of SSP-based FWM processes. Loss1, loss2, and loss3 emulate three types of losses in atom vapor cell, detectors, and feedback loop, respectively.

where the matrix element A_{ij} (i, $j = 1, 2, 3, 4, 5$, and 6) can be found in the Appendix. In this CFC structure, a linear beam splitter (BS) with tunable reflectivity k serves as the feedback strength controller, which feeds part of the output field back into the corresponding input port. The created conjugate beam $\hat{b}_2$ is split into two parts by this BS. One ($\hat{b}_{22}$) is transmitted back to the input port of $\hat{b}_{20}$ and the other ($\hat{b}_{21}$) is the final output field, as shown in Fig. 2. The input-output relationship of the BS controller can be written as

$$\begin{aligned}\hat{b}_{21} &= \sqrt{1-k}\hat{b}_2 + \sqrt{k}\hat{v}_{30},\\ \hat{b}_{22} &= -\sqrt{k}\hat{b}_2 + \sqrt{1-k}\hat{v}_{30},\\ \hat{b}_{20} &= e^{i\phi}\hat{b}_{22},\end{aligned} \tag{3}$$

where k is the reflectivity of the BS, ϕ is the propagation-induced phase delay of the feedback path, and $\hat{v}_{30}$ is the BS-invited vacuum state. Through Eqs. (2) and (3), the relation between the six input fields ($\hat{a}_{10}$, $\hat{b}^{\dagger}_{10}$, $\hat{v}^{\dagger}_{30}$, $\hat{b}^{\dagger}_{30}$, $\hat{a}_{20}$, and $\hat{a}_{30}$) and six output fields ($\hat{a}_1$, $\hat{b}^{\dagger}_1$, $\hat{b}^{\dagger}_{21}$, $\hat{b}^{\dagger}_3$, $\hat{a}_2$, and $\hat{a}_3$) can be obtained by eliminating the intermediate operators $\hat{b}^{\dagger}_2$, $\hat{b}^{\dagger}_{20}$, and $\hat{b}^{\dagger}_{22}$, and be restated as

$$\begin{pmatrix}\hat{a}_1\\ \hat{b}^{\dagger}_1\\ \hat{b}^{\dagger}_{21}\\ \hat{b}^{\dagger}_3\\ \hat{a}_2\\ \hat{a}_3\end{pmatrix} = B\begin{pmatrix}\hat{a}_{10}\\ \hat{b}^{\dagger}_{10}\\ \hat{v}^{\dagger}_{30}\\ \hat{b}^{\dagger}_{30}\\ \hat{a}_{20}\\ \hat{a}_{30}\end{pmatrix}, \tag{4}$$

where the matrix element B_{ij} (i, $j = 1, 2, 3, \ldots, 6$) is given in the Appendix.

In reality, optical loss or imperfect detection efficiencies are inevitable; even worse, they undermine multipartite quantum correlation and entanglement properties. Therefore, for practicality, we take the absorption loss in the atoms, beam transmission loss in the feedback loop, and detection loss in the detectors into consideration, as shown in Fig. 2. To simplify calculation, we harness a BS model to emulate the loss [34] via introducing a vacuum state into each probe beam and conjugate beam. The annihilation operators of vacuum states introduced by the losses from Rb vapor cell absorption are denoted as $\hat{v}_i$ ($i = 1, 2, 3, \ldots, 6$) and that brought in by the feedback path is tagged as $\hat{v}_{32}$. Therefore,

$$\begin{aligned}\hat{a}_1(t) &\to \sqrt{\zeta_1}\hat{a}_1 + \sqrt{1-\zeta_1}\hat{v}_1,\\ \hat{b}_1(t) &\to \sqrt{\zeta_2}\hat{b}_1 + \sqrt{1-\zeta_2}\hat{v}_2,\\ \hat{b}_2(t) &\to \sqrt{\zeta_3}\hat{b}_2 + \sqrt{1-\zeta_3}\hat{v}_3,\\ \hat{b}_3(t) &\to \sqrt{\zeta_4}\hat{b}_3 + \sqrt{1-\zeta_4}\hat{v}_4,\\ \hat{a}_2(t) &\to \sqrt{\zeta_5}\hat{a}_2 + \sqrt{1-\zeta_5}\hat{v}_5,\\ \hat{a}_3(t) &\to \sqrt{\zeta_6}\hat{a}_3 + \sqrt{1-\zeta_6}\hat{v}_6,\\ \hat{b}_{22}(t) &\to \sqrt{\eta}\hat{b}_{22} + \sqrt{1-\eta}\hat{v}_{32},\end{aligned} \tag{5}$$

where η is the optical propagation efficiency of the feedback loop, and ζ_i ($i = 1, 2, 3, \ldots, 6$) is the propagation efficiency in the Rb vapor cell. Due to the short length of the atomic vapor cell (≈ 12 mm) and the small angle between each beam (≈ 8 mrad), the discrepancy in the propagation paths within the cell is negligible. Consequently, the impact of different propagation angles on propagation efficiency can be ignored. However, the different detuning of the three probe beams and three conjugate beams with respect to the ^{85}Rb D_1 line transition results in different atomic absorption losses. The probe beams are nearer to the atomic resonance energy level, resulting in stronger absorption loss relative to conjugate beams. Generally, the propagation efficiency of the probe beam is 0.9, whereas it is 0.95 for the conjugate beam [23]. In this sense, it can be reasonably approximated that $\zeta_1 = \zeta_5 = \zeta_6 = \zeta_a$ for the probe beams and $\zeta_2 = \zeta_3 = \zeta_4 = \zeta_b$ for the conjugate beams. The annihilation operator of the vacuum state given by the loss from the detector is marked as $\hat{v}_i$ ($i = 11$, 21, 31, 41, 51, and 61). Then

$$\begin{aligned}\hat{a}_1(t) &\to \sqrt{\xi_1}\hat{a}_1 + \sqrt{1-\xi_1}\hat{v}_{11},\\ \hat{b}_1(t) &\to \sqrt{\xi_2}\hat{b}_1 + \sqrt{1-\xi_2}\hat{v}_{21},\\ \hat{b}_{21}(t) &\to \sqrt{\xi_3}\hat{b}_{21} + \sqrt{1-\xi_3}\hat{v}_{31},\\ \hat{b}_3(t) &\to \sqrt{\xi_4}\hat{b}_3 + \sqrt{1-\xi_4}\hat{v}_{41},\\ \hat{a}_2(t) &\to \sqrt{\xi_5}\hat{a}_2 + \sqrt{1-\xi_5}\hat{v}_{51},\\ \hat{a}_3(t) &\to \sqrt{\xi_6}\hat{b}_3 + \sqrt{1-\xi_6}\hat{v}_{61}.\end{aligned} \tag{6}$$

Assume that all the detection efficiencies ($\xi_i, i = 1, 2, 3, \ldots, 6$) each have an equal level ξ. Ultimately, the relation between the 19 input fields ($\hat{a}_{10}$, $\hat{b}^{\dagger}_{10}$, $\hat{v}^{\dagger}_{30}$, $\hat{b}^{\dagger}_{30}$, $\hat{a}_{20}$, $\hat{a}_{30}$, $\hat{v}_1$, $\hat{v}^{\dagger}_2$, $\hat{v}^{\dagger}_3$, $\hat{v}^{\dagger}_4$, $\hat{v}_5$, $\hat{v}_6$, $\hat{v}_{11}$, $\hat{v}^{\dagger}_{21}$, $\hat{v}^{\dagger}_{31}$, $\hat{v}^{\dagger}_{41}$, $\hat{v}_{51}$, $\hat{v}_{61}$, and $\hat{v}^{\dagger}_{32}$) and six output fields ($\hat{a}_1$, $\hat{b}^{\dagger}_1$, $\hat{b}^{\dagger}_{21}$, $\hat{b}^{\dagger}_3$, $\hat{a}_2$, and $\hat{a}_3$), via eliminating intermediate

variables, is presented as

$$\begin{pmatrix} \hat{a}_1 \\ \hat{b}_1^\dagger \\ \hat{b}_{21}^\dagger \\ \hat{b}_3^\dagger \\ \hat{a}_2 \\ \hat{a}_3 \end{pmatrix} = K_c C \begin{pmatrix} \hat{a}_{10} \\ \hat{b}_{10}^\dagger \\ \hat{v}_{30}^\dagger \\ \hat{b}_{30}^\dagger \\ \hat{a}_{20} \\ \hat{a}_{30} \\ \hat{v}_1 \\ \hat{v}_2^\dagger \\ \hat{v}_3^\dagger \\ \hat{v}_4^\dagger \\ \hat{v}_5 \\ \hat{v}_6 \\ \hat{v}_{11} \\ \hat{v}_{21}^\dagger \\ \hat{v}_{31}^\dagger \\ \hat{v}_{41}^\dagger \\ \hat{v}_{51} \\ \hat{v}_{61} \\ \hat{v}_{32}^\dagger \end{pmatrix}, \tag{7}$$

where the coefficient K_c and matrix element C_{ij} ($i = 1, 2, 3, \ldots, 6$ and $j = 1, 2, 3, \ldots, 19$) are complicated, as shown in the Appendix.

III. QUANTUM CORRELATION

Now, we focus on the quantum correlation between the six output fields. For convenience, we label the output probe beams $\hat{a}_1$, $\hat{a}_2$, and $\hat{a}_3$ of the CFC system as numbers 1, 5, and 6, respectively. Similarly, the output conjugate beams $\hat{b}_1$, $\hat{b}_{21}$, and $\hat{b}_3$ are numbered as 2, 3, and 4, respectively. Therefore, the photon number operators of the six output beams can be expressed as $\hat{N}_1 = \hat{a}_1^\dagger \hat{a}_1$, $\hat{N}_2 = \hat{b}_1^\dagger \hat{b}_1$, $\hat{N}_3 = \hat{b}_{21}^\dagger \hat{b}_{21}$, $\hat{N}_4 = \hat{b}_3^\dagger \hat{b}_3$, $\hat{N}_5 = \hat{a}_2^\dagger \hat{a}_2$, and $\hat{N}_6 = \hat{a}_3^\dagger \hat{a}_3$, respectively. Hence, the operator for the photon number sum of the probe and conjugate beams is

$$\hat{N} = \hat{N}_1 + \hat{N}_2 + \hat{N}_3 + \hat{N}_4 + \hat{N}_5 + \hat{N}_6, \tag{8}$$

and the difference is

$$\hat{Z} = \hat{N}_1 - \hat{N}_2 - \hat{N}_3 - \hat{N}_4 + \hat{N}_5 + \hat{N}_6. \tag{9}$$

The quantum correlation of the six output fields can be characterized by the degree of the IDS, which can be defined as the ratio of variance for the intensity-difference photon number operator of the six output beams to the variance at the standard quantum limit (SQL). Then the degree of the IDS (D, in units of dB) can be written as

$$\begin{aligned} D_{123456} &= 10 \log_{10} \frac{\mathrm{Var}(\hat{Z})}{\mathrm{Var}(\hat{Z})_{\mathrm{SQL}}} \\ &= 10 \log_{10} \frac{\mathrm{Var}(\hat{Z})}{\langle \hat{N} \rangle}. \end{aligned} \tag{10}$$

Through Eqs. (7)–(10), the D of this CFC system can be calculated. Subsequently, we can analyze the dependence of D_{123456} on the reflectivity k of the BS, phase ϕ, and FWM interaction time t.

At first, we set the transmission efficiencies in the vapor cell $\zeta_a = 0.9$ and $\zeta_b = 0.95$, in the feedback loop $\eta = 0.98$, and in the detector $\xi = 0.9$. The FWM interaction strengths are set as $\varepsilon_1 = 1$, $\varepsilon_2 = 5$, and $\varepsilon_6 = 0.4$, respectively. Figure 3 describes how the feedback strength k and phase ϕ affect the D_{123456} when interaction time t is set to 0.1, 0.2, and 0.3, respectively. It is worth noting that the increase in interaction time t corresponds to increase in pump power in the system. As shown in Figs. 3(a)–3(c), when the phase ϕ and feedback ratio k are set within a suitable range, the value of D_{123456} is smaller than that of the case with $k = 0$ (i.e., no feedback), which indicates that the hexapartite quantum correlation is enhanced. However, it can be observed that excessive feedback leads to the disappearance of hexapartite quantum correlation enhancement, even the disappearance of hexapartite quantum correlation. Additionally, as shown in Figs. 3(a)–3(c), the squeezing enhancement area shrinks with increasing t. This is because, when D is higher, the whole system will be more sensitive to loss [35].

Furthermore, the phase introduced by the feedback process makes the non-phase-sensitive FWM system into a phase-sensitive one. As shown in Figs. 3(a)–3(c), the minimum of D_{123456} is obtained when $\phi = \pi$ before sharp antisqueezing peaks appear. To verify the reason why minimum occurs at a phase of π, as shown in Fig. 4, we depict the intensity of the six output fields ($\hat{N}_i$, $i = 1, 2, 3, \ldots, 6$) of the CFC system changing with the phase due to the interference effects, and find that the CFC system obtains the maximum field intensity gain at $\phi = \pi$, which is consistent with Ref. [36]. However vacuum noise $\hat{v}_{30}$ induced by the controlling BS is also amplified at this phase.

To analyze the optimal feedback strength, we plot the curve of D_{123456} versus reflectivity k when phase is fixed to π, as shown in Fig. 5(a). For analysis, the giant antisqueezing peaks as mentioned above and their subsequent curves were omitted in Fig. 5(b). The traces in different lines represent different values of t in Figs. 5(a) and 5(b), and the corresponding dotted horizontal dashed lines represent the feedback-free D_{123456}.

Clearly, there always exists a feedback ratio domain in which D_{123456} is reduced, that is, we can adjust reflectivity to manipulate and even enhance the degree of quantum correlation between the six output beams. Furthermore, there is always an optimal feedback ratio that maximizes the squeezing under different gain conditions as a result of the balance between the two mechanisms, feedback gain and the vacuum noise [24]. In detail, when k is small, the gain mechanism arising from the feedback of the conjugate beam suppresses the degradation caused by the vacuum noise from the BS controller, so the quantum correlation increases as k goes up. As the growth in k continues, the competition outcome will be reversed, thus the quantum correlation will decline. At the competitive equilibrium point, the squeezing enhancement of hexapartite correlation reaches a maximum of 3.32, 2.47, and 0.45 dB when $k = 0.56$, 0.25, and 0.02, respectively, for the cases of $t = 0.1$, 0.2, and 0.3, respectively, as shown in Fig. 5(b).

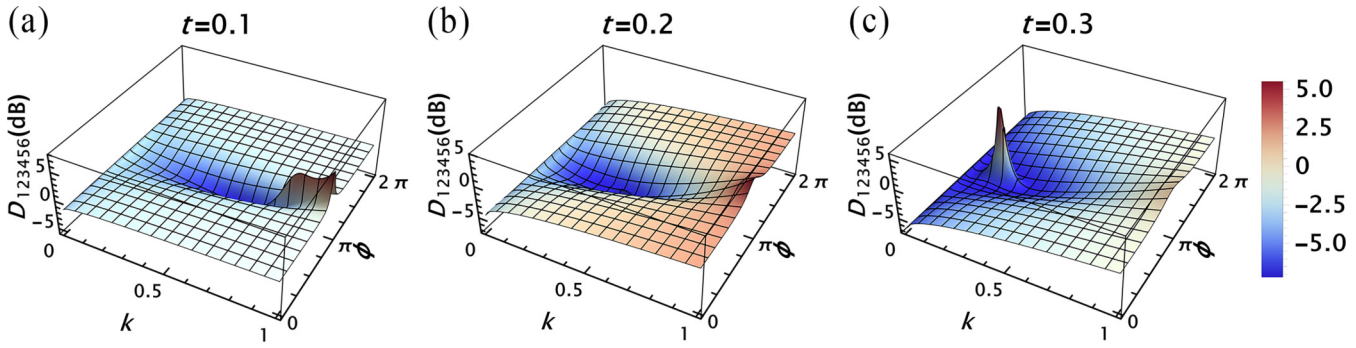

FIG. 3. D_{123456} as a function of feedback ratio k and phase ϕ is examined when $\zeta_a = 0.9$, $\zeta_b = 0.95$, $\eta = 0.98$, $\xi = 0.9$, and interaction strength $\varepsilon_1 = 1$, $\varepsilon_2 = 5$, and $\varepsilon_6 = 0.4$. (a) The interaction time $t = 0.1$. The D_{123456} reaches maximum -5.07 dB when $k = 0.56$ and $\phi = \pi$. (b) The interaction time $t = 0.2$. The D_{123456} gets its maximum value of -7.23 dB when $k = 0.25$ and $\phi = \pi$. (c) The interaction time $t = 0.3$. The maximum of D_{123456} achieves -7.24 dB when $k = 0.02$ and $\phi = \pi$.

In order to better illustrate the relationship between the correlation enhancement and intensity gain of the system, we draw the curves of D_{123456} with intensity gain under the case without feedback and with feedback, respectively, as shown in Fig. 6, where the case with feedback takes the minimum value of D_{123456} at the corresponding t. Due to the presence of asymmetric losses in the system, i.e., the disparity in atomic absorption losses between the probe and the conjugate beams, D_{123456} approaches its threshold value of -7.24 dB as t increases. As can be seen from Fig. 6, the degree of the correlation enhancement increases first and then decreases, with a maximum of 3.54 dB at $t = 0.14$. This is due to the fact that when the initial nonlinear interaction strength is weak, i.e., the value of t is small, the feedback effect is predominant, making the correlation enhancement gradually significant. As t increases, the D_{123456} in the absence of feedback becomes strong, whereas the impact of feedback gradually diminishes due to the inherent losses within the system.

IV. QUANTUM ENTANGLEMENT

In this section, we turn to investigate the entanglement characteristics of the CFC system discussed above. A quantum state can be characterized by its amplitude and phase quadrature operators in the field of continuous variables. We have derived the relation between the inputs and outputs in Sec. II. Then the six output beams of this system can be depicted as

$$\begin{aligned}
\hat{X}_1 &= (\hat{a}_1 + \hat{a}_1^\dagger), \quad \hat{Y}_1 = i(\hat{a}_1^\dagger - \hat{a}_1),\\
\hat{X}_2 &= (\hat{b}_1 + \hat{b}_1^\dagger), \quad \hat{Y}_2 = i(\hat{b}_1^\dagger - \hat{b}_1),\\
\hat{X}_3 &= (\hat{b}_{21} + \hat{b}_{21}^\dagger), \quad \hat{Y}_3 = i(\hat{b}_{21}^\dagger - \hat{b}_{21}),\\
\hat{X}_4 &= (\hat{b}_3 + \hat{b}_3^\dagger), \quad \hat{Y}_4 = i(\hat{b}_3^\dagger - \hat{b}_3),\\
\hat{X}_5 &= (\hat{a}_2 + \hat{a}_2^\dagger), \quad \hat{Y}_5 = i(\hat{a}_2^\dagger - \hat{a}_2),\\
\hat{X}_6 &= (\hat{a}_3 + \hat{a}_3^\dagger), \quad \hat{Y}_6 = i(\hat{a}_3^\dagger - \hat{a}_3),
\end{aligned} \tag{11}$$

where the amplitude and phase quadrature operators obey the commutation relation $[\hat{X}_m, \hat{Y}_m] = 2i$. The quantum entanglement property of the state can be fully described by its covariance matrix (CM). The covariance of the amplitude quadrature operator is defined as $\langle \hat{X}_m \hat{X}_n \rangle = \langle \hat{X}_m \hat{X}_n + \hat{X}_n \hat{X}_m \rangle / 2 - \langle \hat{X}_m \rangle \langle \hat{X}_n \rangle$ $(m, n = 1, 2, 3, \ldots, 6)$. Similarly, the covariance of the phase quadrature operator can also be acquired. The CM of this system is equal to

$$\begin{pmatrix}
\langle \hat{X}_1^2 \rangle & \langle \hat{X}_1 \hat{X}_2 \rangle & \cdots & 0 & 0\\
\langle \hat{X}_2 \hat{X}_1 \rangle & \langle \hat{X}_2^2 \rangle & \cdots & 0 & 0\\
\vdots & \vdots & \ddots & \vdots & \vdots\\
0 & 0 & \cdots & \langle \hat{Y}_5^2 \rangle & \langle \hat{Y}_5 \hat{Y}_6 \rangle\\
0 & 0 & \cdots & \langle \hat{Y}_6 \hat{Y}_5 \rangle & \langle \hat{Y}_6^2 \rangle
\end{pmatrix}, \tag{12}$$

where $\langle \hat{X}_m \hat{Y}_n \rangle = 0$ $(m, n = 1, 2, 3, \ldots, 6)$.

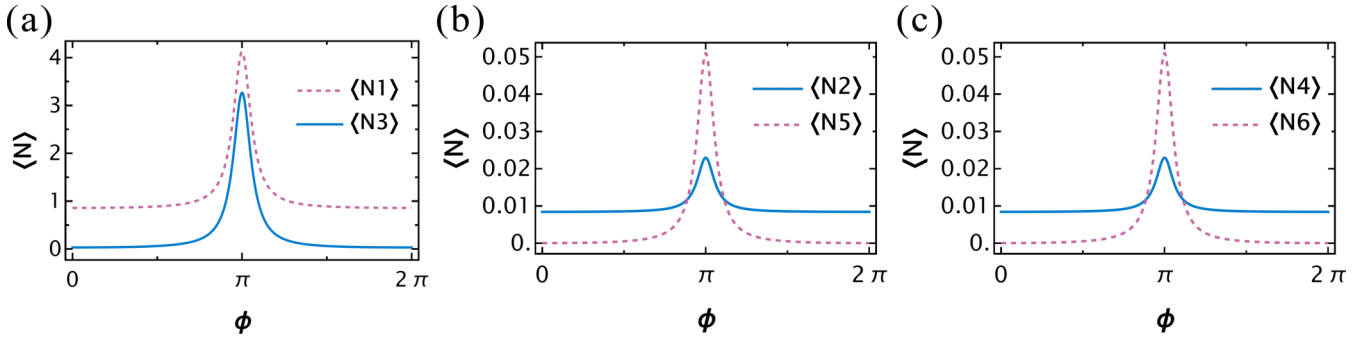

FIG. 4. Intensity of six output fields is plotted as a function of phase ϕ when feedback ratio $k = 0.56$, interaction time $t = 0.1$, $\zeta_a = 0.9$, $\zeta_b = 0.95$, $\eta = 0.98$, $\xi = 0.9$, and interaction strength $\varepsilon_1 = 1$, $\varepsilon_2 = 5$, and $\varepsilon_6 = 0.4$. (a) The intensity of $\hat{a}_1$ and $\hat{b}_2$. (b) The intensity of $\hat{a}_2$ and $\hat{b}_1$. (c) The intensity of $\hat{a}_3$ and $\hat{b}_3$.

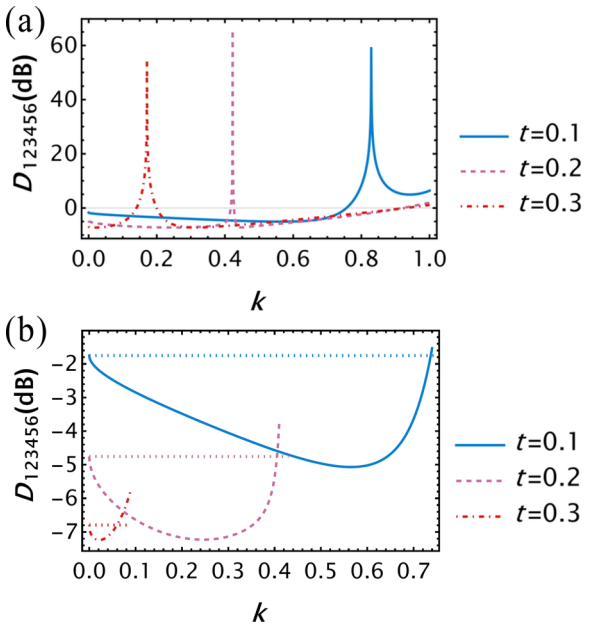

FIG. 5. (a) The value of D_{123456} varies with the feedback strength k and interaction time t when the phase is set to π, $\zeta_a = 0.9$, $\zeta_b = 0.95$, $\eta = 0.98$, $\xi = 0.9$, $\varepsilon_1 = 1$, $\varepsilon_2 = 5$, and $\varepsilon_6 = 0.4$. (b) A partial magnified view of (a). The dotted horizontal lines represent the values of D_{123456} without feedback.

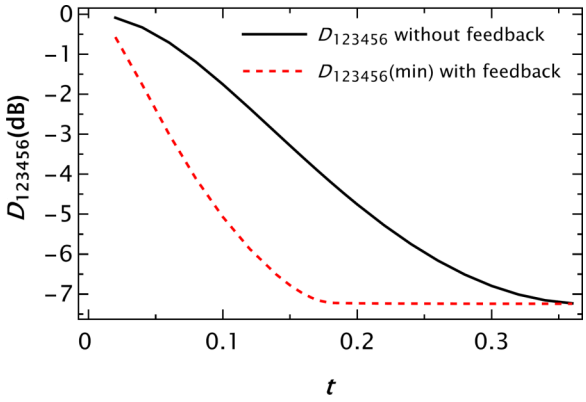

FIG. 6. The evolution of D_{123456} with interaction time t for both scenarios without feedback (solid line) and with feedback (dashed line) when the phase is set to π, $\zeta_a = 0.9$, $\zeta_b = 0.95$, $\eta = 0.98$, $\xi = 0.9$, $\varepsilon_1 = 1$, $\varepsilon_2 = 5$, and $\varepsilon_6 = 0.4$.

The PPT criterion [29–31] is a sufficient criterion to characterize multipartite entanglement. If all the smallest symplectic eigenvalues of the transposed CMs of a whole system are smaller than 1, it indicates the existence of multipartite entanglement in this system. For a N-partite state, we need to confirm $2^{N-1} - 1$ possible bipartitions. There are three types of possible partial transposed (PT) operations of 1×5, 2×4, and 3×3 for the hexapartite state generated by the CFC SSP-based FWM processes, and the total number of bipartitions is 31. As mentioned earlier, if the smallest symplectic eigenvalues of the 31 bipartitions are all less than 1, it can be proven that the system produces a fully hexapartite entangled state. Moreover, the smaller the smallest symplectic eigenvalue, the stronger the entanglement [37]. Next, we still set $\zeta_a = 0.9$, $\zeta_b = 0.95$, $\eta = 0.98$, $\xi = 0.9$, $\varepsilon_1 = 1$, $\varepsilon_2 = 5$, $\varepsilon_6 = 0.4$, and $t = 0.1$ to investigate the smallest symplectic eigenvalues as a function of phase and reflectivity under the loss for all of the 31 bipartitions.

First, when applying PT operation to one beam, the results are shown in Fig. 7. Six 1×5 bipartitions

$\hat{a}_1 \mid (\hat{b}_1, \hat{b}_{21}, \hat{b}_3, \hat{a}_2, \hat{a}_3)$, $\hat{b}_1 \mid (\hat{a}_1, \hat{b}_{21}, \hat{b}_3, \hat{a}_2, \hat{a}_3)$,
$\hat{b}_{21} \mid (\hat{a}_1, \hat{b}_1, \hat{b}_3, \hat{a}_2, \hat{a}_3)$, $\hat{b}_3 \mid (\hat{a}_1, \hat{b}_1, \hat{b}_{21}, \hat{a}_2, \hat{a}_3)$,
$\hat{a}_2 \mid (\hat{a}_1, \hat{b}_1, \hat{b}_{21}, \hat{b}_3, \hat{a}_3)$, and $\hat{a}_3 \mid (\hat{a}_1, \hat{b}_1, \hat{b}_{21}, \hat{b}_3, \hat{a}_2)$

are depicted in Figs. 7(a)–7(f), respectively. The value on each contour represents the smallest symplectic eigenvalue. It can be concluded that all the six 1×5 bipartitions are fully inseparable with the increasing reflectivity and phase, as the smallest symplectic eigenvalues are all smaller than 1. Moreover, as drawn in Fig. 7(a), with the circumstance of $\phi = \pi$, the entanglement between $\hat{a}_1$ and $(\hat{b}_1, \hat{b}_{21}, \hat{b}_3, \hat{a}_2, \hat{a}_3)$ is significantly enhanced when the reflectivity is between 0.3 and 0.9 compared to the case without feedback. As shown in Fig. 7(c), the similar situation can also be seen between $\hat{b}_{21}$ and $(\hat{a}_1, \hat{b}_1, \hat{b}_3, \hat{a}_2, \hat{a}_3)$. In addition, as shown in Figs. 7(e) and 7(f), when $\phi = \pi$ and k is in the range of 0.3–0.8, there is also a clear entanglement enhancement in corresponding bipartitions. However, when phase is equal to π, the entanglement between $\hat{b}_1$ and $(\hat{a}_1, \hat{b}_{21}, \hat{b}_3, \hat{a}_2, \hat{a}_3)$ is weakened as the reflectivity increases compared to the no-feedback case, as shown in Fig. 7(b). A similar case occurs between $\hat{b}_3$ and $(\hat{a}_1, \hat{b}_1, \hat{b}_{21}, \hat{a}_2, \hat{a}_3)$, as shown in Fig. 7(d).

Second, when the PT operation is employed in two beams, 15 2×4 bipartitions

$(\hat{a}_1, \hat{b}_1) \mid (\hat{b}_{21}, \hat{b}_3, \hat{a}_2, \hat{a}_3)$, $(\hat{a}_1, \hat{b}_{21}) \mid (\hat{b}_1, \hat{b}_3, \hat{a}_2, \hat{a}_3)$,
$(\hat{a}_1, \hat{b}_3) \mid (\hat{b}_1, \hat{b}_{21}, \hat{a}_2, \hat{a}_3)$, $(\hat{a}_1, \hat{a}_2) \mid (\hat{b}_1, \hat{b}_{21}, \hat{b}_3, \hat{a}_3)$,
$(\hat{a}_1, \hat{a}_3) \mid (\hat{b}_1, \hat{b}_{21}, \hat{b}_3, \hat{a}_2)$, $(\hat{b}_1, \hat{b}_{21}) \mid (\hat{a}_1, \hat{b}_3, \hat{a}_2, \hat{a}_3)$,
$(\hat{b}_1, \hat{b}_3) \mid (\hat{a}_1, \hat{b}_{21}, \hat{a}_2, \hat{a}_3)$, $(\hat{b}_1, \hat{a}_2) \mid (\hat{a}_1, \hat{b}_{21}, \hat{b}_3, \hat{a}_3)$,
$(\hat{b}_1, \hat{a}_3) \mid (\hat{a}_1, \hat{b}_{21}, \hat{b}_3, \hat{a}_2)$, $(\hat{b}_{21}, \hat{b}_3) \mid (\hat{a}_1, \hat{b}_1, \hat{a}_2, \hat{a}_3)$,
$(\hat{b}_{21}, \hat{a}_2) \mid (\hat{a}_1, \hat{b}_1, \hat{b}_3, \hat{a}_3)$, $(\hat{b}_{21}, \hat{a}_3) \mid (\hat{a}_1, \hat{b}_1, \hat{b}_3, \hat{a}_2)$,
$(\hat{b}_3, \hat{a}_2) \mid (\hat{a}_1, \hat{b}_1, \hat{b}_{21}, \hat{a}_3)$, $(\hat{b}_3, \hat{a}_3) \mid (\hat{a}_1, \hat{b}_1, \hat{b}_{21}, \hat{a}_2)$,

and $(\hat{a}_2, \hat{a}_3) \mid (\hat{a}_1, \hat{b}_1, \hat{b}_{21}, \hat{b}_3)$ are depicted in Figs. 8(a)–8(o), respectively. When phase is set to π and reflectivity is in the range of 0.4–0.75, there still exists obvious entanglement enhancement, as shown in Figs. 8(a)–8(f) and 8(h)–8(o). However, under the same condition, the entanglement between $(\hat{b}_1, \hat{b}_3)$ and $(\hat{a}_1, \hat{b}_{21}, \hat{a}_2, \hat{a}_3)$ is weakened, as shown in Fig. 8(g).

Finally, the PT operation is utilized in three beams. The corresponding ten 3×3 bipartitions

$(\hat{a}_1, \hat{b}_1, \hat{b}_{21}) \mid (\hat{b}_3, \hat{a}_2, \hat{a}_3)$, $(\hat{a}_1, \hat{b}_1, \hat{b}_3) \mid (\hat{b}_{21}, \hat{a}_2, \hat{a}_3)$,
$(\hat{a}_1, \hat{b}_1, \hat{a}_2) \mid (\hat{b}_{21}, \hat{b}_3, \hat{a}_3)$, $(\hat{a}_1, \hat{b}_1, \hat{a}_3) \mid (\hat{b}_{21}, \hat{b}_3, \hat{a}_2)$,
$(\hat{a}_1, \hat{b}_{21}, \hat{b}_3) \mid (\hat{b}_1, \hat{a}_2, \hat{a}_3)$, $(\hat{a}_1, \hat{b}_{21}, \hat{a}_2) \mid (\hat{b}_1, \hat{b}_3, \hat{a}_3)$,
$(\hat{a}_1, \hat{b}_{21}, \hat{a}_3) \mid (\hat{b}_1, \hat{b}_3, \hat{a}_2)$, $(\hat{a}_1, \hat{b}_3, \hat{a}_2) \mid (\hat{b}_1, \hat{b}_{21}, \hat{a}_3)$,
$(\hat{a}_1, \hat{b}_3, \hat{a}_3) \mid (\hat{b}_1, \hat{b}_{21}, \hat{a}_2)$, and $(\hat{a}_1, \hat{a}_2, \hat{a}_3) \mid (\hat{b}_1, \hat{b}_{21}, \hat{b}_3)$

are depicted in Figs. 9(a)–9(j), respectively. Entanglement enhancement is witnessed in all 3×3 bipartitions when phase is equal to π and reflectivity is in the range of 0.55–0.75.

Based on the above analysis, we can see that all of the 31 possible bipartitions are still entangled after feedback and the entanglement structure characterized by the symplectic eigenvalues can be tailored by adjusting reflectivity and phase. In our feedback structure, the output conjugate beam $\hat{b}_2$ from the FWM processes is partially transmitted back

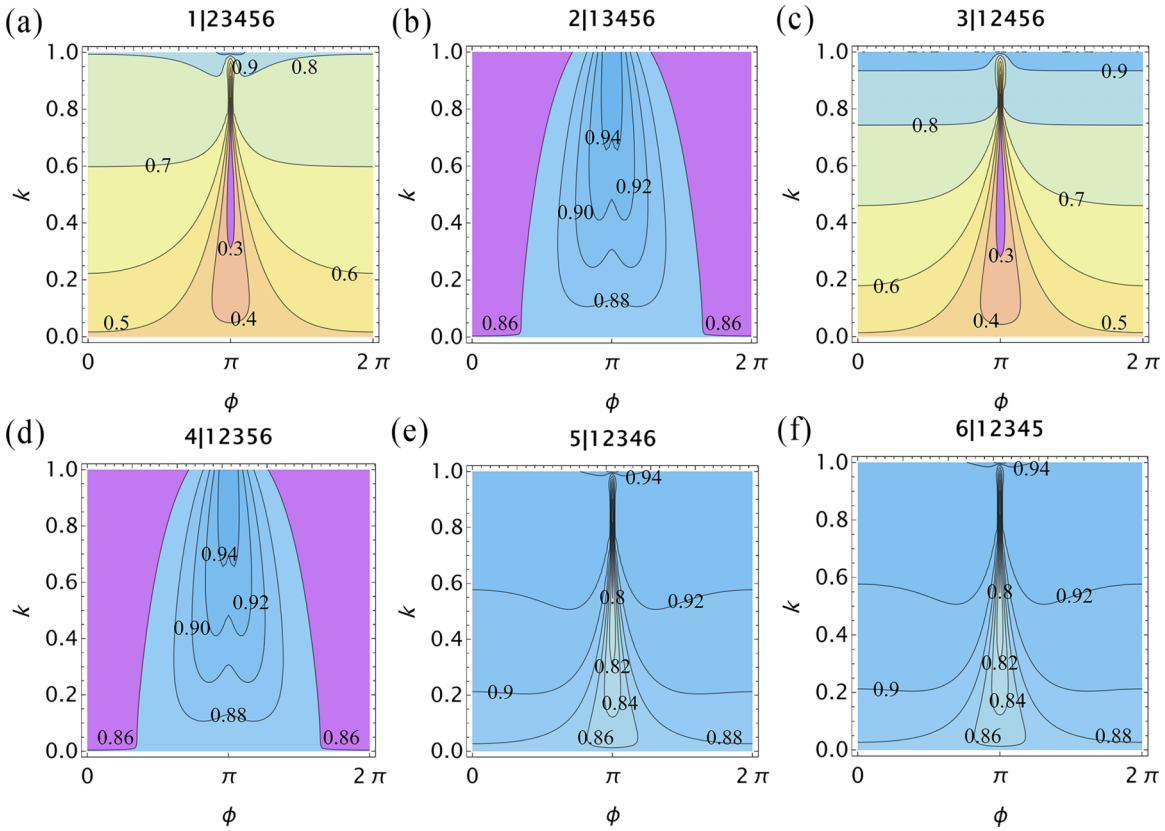

FIG. 7. Corresponding smallest symplectic eigenvalues of all the six 1×5 bipartitions varying with phase and reflectivity: (a) $\hat{a}_1$ | $(\hat{b}_1, \hat{b}_{21}, \hat{b}_3, \hat{a}_2, \hat{a}_3)$, (b) $\hat{b}_1$ | $(\hat{a}_1, \hat{b}_{21}, \hat{b}_3, \hat{a}_2, \hat{a}_3)$, (c) $\hat{b}_{21}$ | $(\hat{a}_1, \hat{b}_1, \hat{b}_3, \hat{a}_2, \hat{a}_3)$, (d) $\hat{b}_3$ | $(\hat{a}_1, \hat{b}_1, \hat{b}_{21}, \hat{a}_2, \hat{a}_3)$, (e) $\hat{a}_2$ | $(\hat{a}_1, \hat{b}_1, \hat{b}_{21}, \hat{b}_3, \hat{a}_3)$, and (f) $\hat{a}_3$ | $(\hat{a}_1, \hat{b}_1, \hat{b}_{21}, \hat{b}_3, \hat{a}_2)$.

into the original FWM vacuum input port, which results in the enhancement of entanglement between $\hat{b}_{21}$ and the other five output beams within the suitable reflectivity and phase range. However, for the other two conjugate beams $\hat{b}_1$ and $\hat{b}_3$, entanglement is weakened beneath the same conditions, as shown in Figs. 7(b), 7(d), and 8(g), corresponding to three bipartitions: $\hat{b}_1$ | $(\hat{a}_1, \hat{b}_{21}, \hat{b}_3, \hat{a}_2, \hat{a}_3)$, $\hat{b}_3$ | $(\hat{a}_1, \hat{b}_1, \hat{b}_{21}, \hat{a}_2, \hat{a}_3)$, and $(\hat{b}_1, \hat{b}_3)$ | $(\hat{a}_1, \hat{b}_{21}, \hat{a}_2, \hat{a}_3)$. For the three special cases, the smallest symplectic eigenvalues keep increasing with k when phase is set to π. Except for the above bipartitions, in the other 28 bipartitions, with k rising, the smallest symplectic eigenvalues first decrease and then increase when ϕ equals to π. Moreover, when $\phi = \pi$, and k is in the range of 0.55–0.75, the smallest symplectic eigenvalue takes the minimum; that is, under this condition, entanglement between these bipartitions can be enhanced.

V. CONCLUSIONS

We have theoretically proposed a hexapartite CFC structure with SSP-based FWM processes by utilizing a BS with tunable reflectivity k as the feedback controller and characterized the quantum correlation and entanglement of the hexapartite states under three different kinds of losses. In our configuration, one of the conjugate beams generated from the SSP-based FWM processes is partially transmitted back into the corresponding original vacuum conjugate input port via the BS controller. We find that in a proper BS reflectivity range, the degree of hexapartite quantum correlation can be considerably improved when phase induced by the feedback loop is equal to π. Furthermore, as the intensity gain increases, the IDS enhancement increases first and then decreases. Further enhancement of the squeezing is possible by imputing a squeezed vacuum state at the $\hat{v}_{30}$ port [38]. In addition, entanglement of the hexapartite state can also be tailored by manipulating phase and BS reflectivity. Our paper paves the way for experimental implementation of CFC-based manipulation of multipartite entangled states for practical applications.

ACKNOWLEDGMENTS

This work was funded by the National Natural Science Foundation of China (Grants No. 1222540, No. 1874155, No. 91436211, No. 11374104, No. 12174110, and No. 62205108); Innovation Program of Shanghai Municipal Education Commission (Grant No. 2021-01-07-00-08-E00100); Program of Shanghai Academic Research Leader (Grant No. 22XD1400700); Basic Research Project of Shanghai Science and Technology Commission (Grant No. 20JC1416100); Natural Science Foundation of Shanghai (Grant No. 17ZR1442900); Minhang Leading Talents (Grant No. 201971); Shanghai Sailing Program (Grant No. 21YF1410800); Natural Science Foundation of Chongqing (Grants No. CSTB2022NSCQ-MSX0893 and No. CSTB2022NSCQ-MSX1435); Shanghai Municipal Science

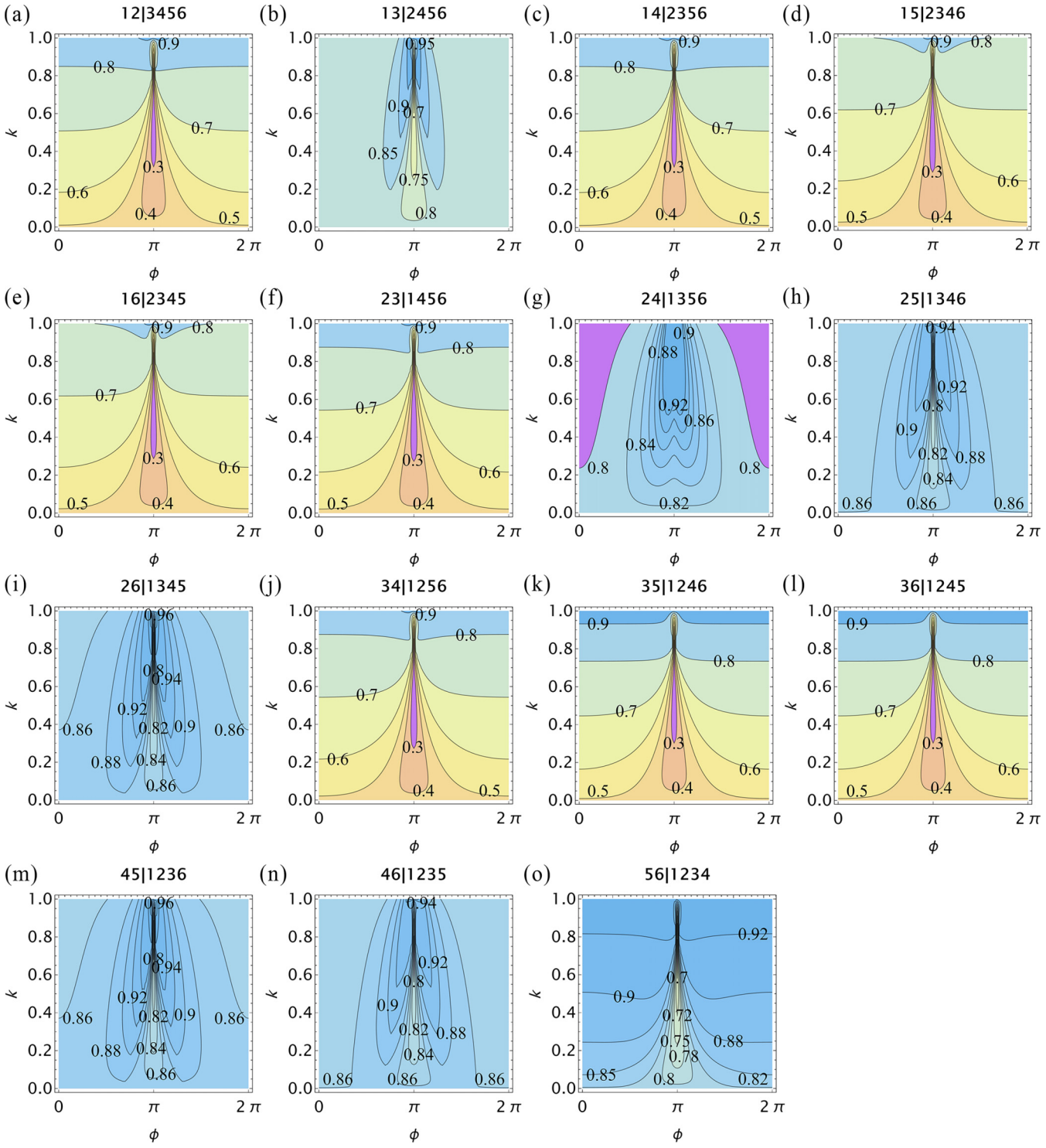

FIG. 8. Smallest symplectic eigenvalues of partially transposed CMs for all 15 2×4 bipartitions are plotted as a function of ϕ and k: (a) $(\hat{a}_1, \hat{b}_1) \mid (\hat{b}_{21}, \hat{b}_3, \hat{a}_2, \hat{a}_3)$, (b) $(\hat{a}_1, \hat{b}_{21}) \mid (\hat{b}_1, \hat{b}_3, \hat{a}_2, \hat{a}_3)$, (c) $(\hat{a}_1, \hat{b}_3) \mid (\hat{b}_1, \hat{b}_{21}, \hat{a}_2, \hat{a}_3)$, (d) $(\hat{a}_1, \hat{a}_2) \mid (\hat{b}_1, \hat{b}_{21}, \hat{b}_3, \hat{a}_3)$, (e) $(\hat{a}_1, \hat{a}_3) \mid (\hat{b}_1, \hat{b}_{21}, \hat{b}_3, \hat{a}_2)$, (f) $(\hat{b}_1, \hat{b}_{21}) \mid (\hat{a}_1, \hat{b}_3, \hat{a}_2, \hat{a}_3)$, (g) $(\hat{b}_1, \hat{b}_3) \mid (\hat{a}_1, \hat{b}_{21}, \hat{a}_2, \hat{a}_3)$, (h) $(\hat{b}_1, \hat{a}_2) \mid (\hat{a}_1, \hat{b}_{21}, \hat{b}_3, \hat{a}_3)$, (i) $(\hat{b}_1, \hat{a}_3) \mid (\hat{a}_1, \hat{b}_{21}, \hat{b}_3, \hat{a}_2)$, (j) $(\hat{b}_{21}, \hat{b}_3) \mid (\hat{a}_1, \hat{b}_1, \hat{a}_3, \hat{a}_2)$, (k) $(\hat{b}_{21}, \hat{a}_2) \mid (\hat{a}_1, \hat{b}_1, \hat{b}_3, \hat{a}_3)$, (l) $(\hat{b}_{21}, \hat{a}_3) \mid (\hat{a}_1, \hat{b}_1, \hat{b}_3, \hat{a}_2)$, (m) $(\hat{b}_3, \hat{a}_2) \mid (\hat{a}_1, \hat{b}_1, \hat{b}_{21}, \hat{a}_3)$, (n) $(\hat{b}_3, \hat{a}_3) \mid (\hat{a}_1, \hat{b}_1, \hat{b}_{21}, \hat{a}_2)$, and (o) $(\hat{a}_2, \hat{a}_3) \mid (\hat{a}_1, \hat{b}_1, \hat{b}_{21}, \hat{b}_3)$.

and Technology Major Project (Grant No. 2019SHZDZX01); and the 111 project (Grant No. B12024).

APPENDIX: MATRIX ELEMENTS OF *A*, *B*, AND *C*

The input-output relationship of the SSP-based FWM processes can be written as Eq. (2) and the matrix element A_{ij}

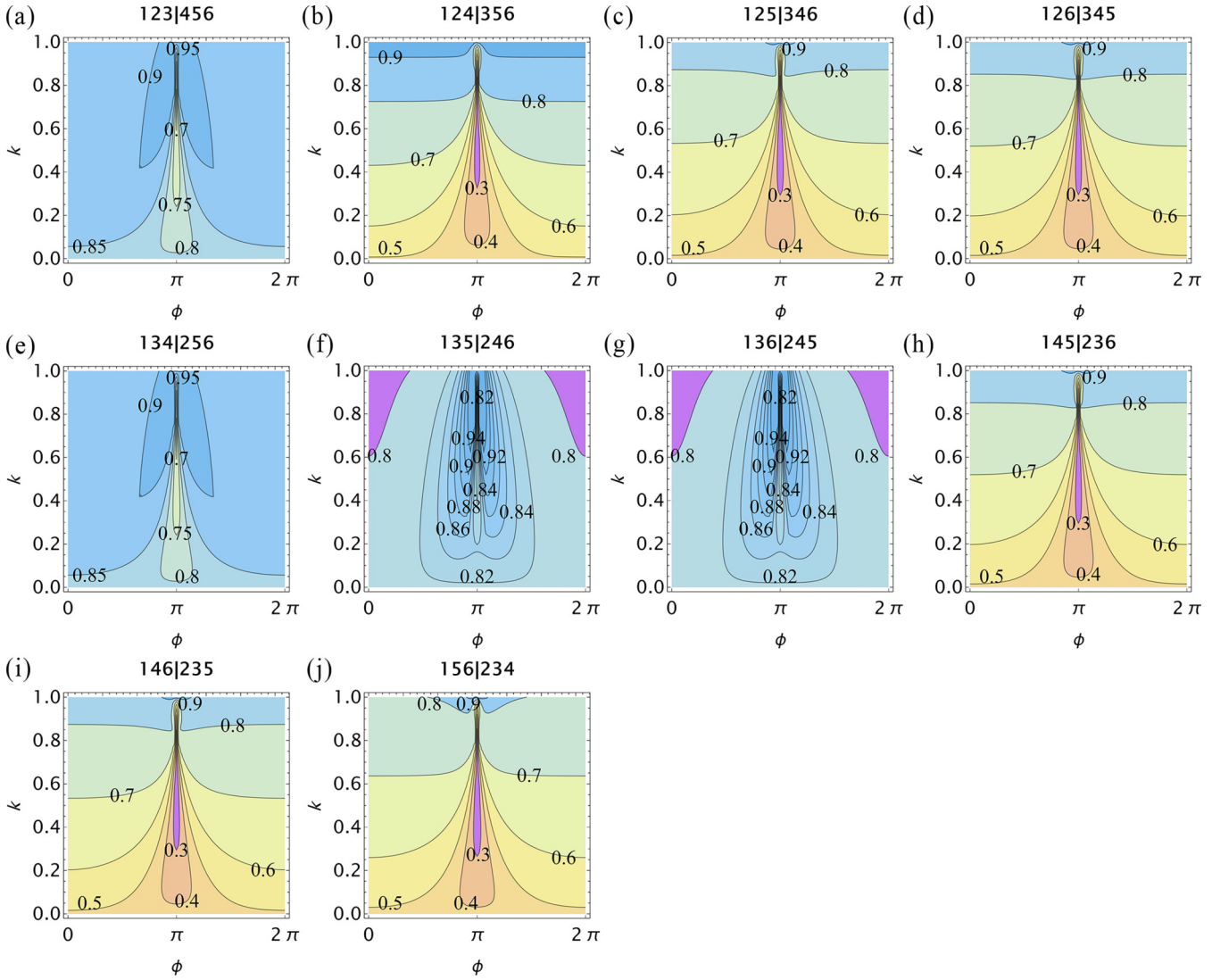

FIG. 9. Corresponding smallest symplectic eigenvalues of all the ten 3 × 3 bipartitions varying with the value of phase and reflectivity, respectively: (a) $(\hat{a}_1, \hat{b}_1, \hat{b}_{21}) \mid (\hat{b}_3, \hat{a}_2, \hat{a}_3)$, (b) $(\hat{a}_1, \hat{b}_1, \hat{b}_3) \mid (\hat{b}_{21}, \hat{a}_2, \hat{a}_3)$, (c) $(\hat{a}_1, \hat{b}_1, \hat{a}_2) \mid (\hat{b}_{21}, \hat{b}_3, \hat{a}_3)$, (d) $(\hat{a}_1, \hat{b}_1, \hat{a}_3) \mid (\hat{b}_{21}, \hat{b}_3, \hat{a}_2)$, (e) $(\hat{a}_1, \hat{b}_{21}, \hat{b}_3) \mid (\hat{b}_1, \hat{a}_2, \hat{a}_3)$, (f) $(\hat{a}_1, \hat{b}_{21}, \hat{a}_2) \mid (\hat{b}_1, \hat{b}_3, \hat{a}_3)$, (g) $(\hat{a}_1, \hat{b}_{21}, \hat{a}_3) \mid (\hat{b}_1, \hat{b}_3, \hat{a}_2)$, (h) $(\hat{a}_1, \hat{b}_3, \hat{a}_2) \mid (\hat{b}_1, \hat{b}_{21}, \hat{a}_3)$, (i) $(\hat{a}_1, \hat{b}_3, \hat{a}_3) \mid (\hat{b}_1, \hat{b}_{21}, \hat{a}_2)$, and (j) $(\hat{a}_1, \hat{a}_2, \hat{a}_3) \mid (\hat{b}_1, \hat{b}_{21}, \hat{b}_3)$.

is as follows:

$$A_{11} = \frac{1}{2\theta}[(\theta-\beta)\cosh(\theta-\alpha)t + (\beta+\theta)\cosh(\alpha+\theta)t],$$

$$A_{12} = \frac{1}{4\theta\varepsilon_1}(\theta^2-\beta^2)[\sinh(\theta-\alpha)t + \sinh(\alpha+\theta)t],$$

$$A_{13} = \frac{1}{2\theta}[(\beta-\theta)\sinh(\theta-\alpha)t + (\beta+\theta)\sinh(\theta+\alpha)t], \quad A_{14} = A_{12},$$

$$A_{15} = \frac{1}{4\theta\varepsilon_1}(\beta^2-\theta^2)[\cosh(\theta-\alpha)t - \cosh(\alpha+\theta)t], \quad A_{16} = A_{15},$$

$$A_{21} = \frac{\varepsilon_1}{2\theta}[\sinh(\theta-\alpha)t + \sinh(\alpha+\theta)t],$$

$$A_{22} = \frac{1}{4\theta}[(\beta+\theta)\cosh(\theta-\alpha)t + (\theta-\beta)\cosh(\alpha+\theta)t + 2\theta\cosh\varepsilon_6 t],$$

$$A_{23} = \frac{\varepsilon_1}{2\theta}[\cosh(\alpha-\theta)t + \cosh(\alpha+\theta)t],$$

$$
\begin{aligned}
A_{24} &= \frac{1}{4\theta}[(\beta+\theta)\cosh(\theta-\alpha)t + (\theta-\beta)\cosh(\alpha+\theta)t - 2\theta\cosh\varepsilon_6 t],\\
A_{25} &= \frac{1}{4\theta}[(\beta+\theta)\sinh(\alpha-\theta)t + (\theta-\beta)\sinh(\alpha+\theta)t - 2\theta\sinh\varepsilon_6 t],\\
A_{26} &= \frac{1}{4\theta}[(\beta+\theta)\sinh(\alpha-\theta)t + (\theta-\beta)\sinh(\alpha+\theta)t + 2\theta\sinh\varepsilon_6 t],\\
&A_{31}=A_{13},\quad A_{32}=A_{15},\quad A_{33}=A_{11},\quad A_{34}=A_{15},\quad A_{35}=A_{36}=A_{12},\\
&A_{41}=A_{21},\quad A_{42}=A_{24},\quad A_{43}=A_{23},\quad A_{44}=A_{22},\quad A_{45}=A_{26},\quad A_{46}=A_{25},\\
&A_{51}=A_{23},\quad A_{52}=A_{25},\quad A_{53}=A_{21},\quad A_{54}=A_{26},\quad A_{55}=A_{22},\quad A_{56}=A_{24},\\
&A_{61}=A_{23},\quad A_{62}=A_{26},\quad A_{63}=A_{21},\quad A_{64}=A_{25},\quad A_{65}=A_{24},\quad A_{66}=A_{22},
\end{aligned}
\tag{A1}
$$

where

$$
\begin{aligned}
\alpha &= (\varepsilon_2+\varepsilon_6)/2,\\
\beta &= (\varepsilon_2-\varepsilon_6)/2,\\
\theta &= \sqrt{2\varepsilon_1^2+\beta^2}.
\end{aligned}
\tag{A2}
$$

The relation between inputs and outputs of the CFC system can be restated as Eq. (4). The detailed matrix element B_{ij} is as follows:

$$
B_{11} = \frac{1}{2\theta}\frac{2e^{i\phi}\theta[\beta+\theta\coth(t\alpha)\coth(t\theta)] + \sqrt{k}[\beta^2+\theta^2-(\beta^2-\theta^2)\cosh(2t\theta)]\operatorname{csch}(t\alpha)\operatorname{csch}(t\theta)}{\sqrt{k}[\beta+\theta\coth(t\alpha)\coth(t\theta)] + e^{i\phi}\theta\operatorname{csch}(t\alpha)\operatorname{csch}(t\theta)},
$$

$$
B_{12} = -\frac{1}{2\varepsilon_1}\frac{(\beta^2-\theta^2)[e^{i\phi}\cosh(t\alpha)+\sqrt{k}\cosh(t\theta)]\operatorname{csch}(t\alpha)}{\sqrt{k}[\beta+\theta\coth(t\alpha)\coth(t\theta)] + e^{i\phi}\theta\operatorname{csch}(t\alpha)\operatorname{csch}(t\theta)},
$$

$$
B_{13} = \frac{\sqrt{1-k}[\beta\coth(t\alpha)+\theta\coth(t\theta)]}{\sqrt{k}[\beta+\theta\coth(t\alpha)\coth(t\theta)] + e^{i\phi}\theta\operatorname{csch}(t\alpha)\operatorname{csch}(t\theta)},\quad B_{14}=B_{12},
$$

$$
B_{15} = \frac{1}{2\varepsilon_1\theta}\frac{(\beta^2-\theta^2)[-e^{i\phi}\theta+\sqrt{k}\beta\operatorname{csch}(t\alpha)\sinh(t\theta)]}{\sqrt{k}[\beta+\theta\coth(t\alpha)\coth(t\theta)] + e^{i\phi}\theta\operatorname{csch}(t\alpha)\operatorname{csch}(t\theta)},\quad B_{16}=B_{15},
$$

$$
B_{21} = \frac{\varepsilon_1[\cosh(t\alpha)+e^{-i\phi}\sqrt{k}\cosh(t\theta)]\sinh(t\theta)}{\theta+e^{-i\phi}\sqrt{k}[\theta\cosh(t\alpha)\cosh(t\theta)+\beta\sinh(t\alpha)\sinh(t\theta)]},
$$

$$
B_{22} = \frac{1}{4}\frac{\left\{\begin{array}{c}2\theta[\cosh(\varepsilon_6 t)+\cosh(t\alpha)\cosh(t\theta)]-2\beta\sinh(t\alpha)\sinh(t\theta)\\ +e^{-i\phi}\sqrt{k}\{\theta\cosh(2t\alpha)+\theta\cosh(2t\theta)+2\cosh(\varepsilon_6 t)[\theta\cosh(t\alpha)\cosh(t\theta)+\beta\sinh(t\alpha)\sinh(t\theta)]\}\end{array}\right\}}{\theta+e^{-i\phi}\sqrt{k}[\theta\cosh(t\alpha)\cosh(t\theta)+\beta\sinh(t\alpha)\sinh(t\theta)]},
$$

$$
B_{23} = \frac{\varepsilon_1 e^{-i\phi}\sqrt{1-k}\sinh(t\alpha)\sinh(t\theta)}{\theta+e^{-i\phi}\sqrt{k}[\theta\cosh(t\alpha)\cosh(t\theta)+\beta\sinh(t\alpha)\sinh(t\theta)]},
$$

$$
B_{24} = \frac{1}{4}\frac{\left\{\begin{array}{c}-2[\theta\cosh(\varepsilon_6 t)-\theta\cosh(t\alpha)\cosh(t\theta)+\beta\sinh(t\alpha)\sinh(t\theta)]\\ +e^{-i\phi}\sqrt{k}\{\theta\cosh(2t\alpha)+\theta\cosh(2t\theta)-2\cosh(\varepsilon_6 t)[\theta\cosh(t\alpha)\cosh(t\theta)+\beta\sinh(t\alpha)\sinh(t\theta)]\}\end{array}\right\}}{\theta+e^{-i\phi}\sqrt{k}[\theta\cosh(t\alpha)\cosh(t\theta)+\beta\sinh(t\alpha)\sinh(t\theta)]},
$$

$$
B_{25} = \frac{1}{2}\frac{\left\{\begin{array}{c}-\theta\sinh(\varepsilon_6 t)+\theta\cosh(t\theta)\sinh(t\alpha)-\beta\cosh(t\alpha)\sinh(t\theta)\\ +e^{-i\phi}\sqrt{k}\{\theta\cosh(t\alpha)[-\cosh(t\theta)\sinh(\varepsilon_6 t)+\sinh(t\alpha)]-\beta[\cosh(t\theta)+\sinh(\varepsilon_6 t)\sinh(t\alpha)]\sinh(t\theta)\}\end{array}\right\}}{\theta+e^{-i\phi}\sqrt{k}[\theta\cosh(t\alpha)\cosh(t\theta)+\beta\sinh(t\alpha)\sinh(t\theta)]},
$$

$$
B_{26} = \frac{1}{2}\frac{\left\{\begin{array}{c}\theta\sinh(\varepsilon_6 t)+\theta\cosh(t\theta)\sinh(t\alpha)-\beta\cosh(t\alpha)\sinh(t\theta)\\ +e^{-i\phi}\sqrt{k}\{\theta\cosh(t\alpha)[\cosh(t\theta)\sinh(\varepsilon_6 t)+\sinh(t\alpha)]+\beta[-\cosh(t\theta)+\sinh(\varepsilon_6 t)\sinh(t\alpha)]\sinh(t\theta)\}\end{array}\right\}}{\theta+e^{-i\phi}\sqrt{k}[\theta\cosh(t\alpha)\cosh(t\theta)+\beta\sinh(t\alpha)\sinh(t\theta)]},
$$

$$
B_{31} = \frac{\sqrt{1-k}[\theta\cosh(t\theta)\sinh(t\alpha)+\beta\cosh(t\alpha)\sinh(t\theta)]}{\theta+e^{-i\phi}\sqrt{k}[\theta\cosh(t\alpha)\cosh(t\theta)+\beta\sinh(t\alpha)\sinh(t\theta)]},
$$

$$
B_{32} = \frac{1}{2\varepsilon_1}\frac{-\sqrt{1-k}(\beta^2-\theta^2)\sinh(t\alpha)\sinh(t\theta)}{\theta+e^{-i\phi}\sqrt{k}[\theta\cosh(t\alpha)\cosh(t\theta)+\beta\sinh(t\alpha)\sinh(t\theta)]},
$$

$$B_{33}=\frac{\sqrt{k}\theta+e^{-i\phi}[\theta\cosh(t\alpha)\cosh(t\theta)+\beta\sinh(t\alpha)\sinh(t\theta)]}{\theta+e^{-i\phi}\sqrt{k}[\theta\cosh(t\alpha)\cosh(t\theta)+\beta\sinh(t\alpha)\sinh(t\theta)]},\quad B_{34}=B_{32},\quad B_{35}=B_{32}\frac{\cosh(t\alpha)}{\sinh(t\alpha)},\quad B_{36}=B_{35},$$

$$B_{41}=B_{21},\quad B_{42}=B_{24},\quad B_{43}=B_{23},\quad B_{44}=B_{22},\quad B_{45}=B_{26},\quad B_{46}=B_{25},$$

$$B_{51}=\frac{1}{\theta}\frac{\varepsilon_1\sinh(t\theta)[\theta\sinh(t\alpha)-e^{-i\phi}\sqrt{k}\beta\sinh(t\theta)]}{\theta+e^{-i\phi}\sqrt{k}[\theta\cosh(t\alpha)\cosh(t\theta)+\beta\sinh(t\alpha)\sinh(t\theta)]},\quad B_{52}=B_{25},\quad B_{53}=B_{23}\frac{\cosh(t\alpha)}{\sinh(t\alpha)},\quad B_{54}=B_{26},$$

$$B_{55}=\frac{1}{4\theta}\frac{\left\{\begin{array}{c}2\theta[\theta\cosh(\varepsilon_6 t)+\theta\cosh(t\alpha)\cosh(t\theta)-\beta\sinh(t\alpha)\sinh(t\theta)]\\+e^{-i\phi}\sqrt{k}\{-\beta^2+\theta^2+\theta^2\cosh(2t\alpha)+\beta^2\cosh(2t\theta)+2\theta\cosh(\varepsilon_6 t)[\theta\cosh(t\alpha)\cosh(t\theta)+\beta\sinh(t\alpha)\sinh(t\theta)]\}\end{array}\right\}}{\theta+e^{-i\phi}\sqrt{k}[\theta\cosh(t\alpha)\cosh(t\theta)+\beta\sinh(t\alpha)\sinh(t\theta)]},$$

$$B_{56}=\frac{1}{4\theta}\frac{\left\{\begin{array}{c}-2\theta[\theta\cosh(\varepsilon_6 t)-\theta\cosh(t\alpha)\cosh(t\theta)+\beta\sinh(t\alpha)\sinh(t\theta)]\\+e^{-i\phi}\sqrt{k}\{-\beta^2+\theta^2+\theta^2\cosh(2t\alpha)+\beta^2\cosh(2t\theta)-2\theta\cosh(\varepsilon_6 t)[\theta\cosh(t\alpha)\cosh(t\theta)+\beta\sinh(t\alpha)\sinh(t\theta)]\}\end{array}\right\}}{\theta+e^{-i\phi}\sqrt{k}[\theta\cosh(t\alpha)\cosh(t\theta)+\beta\sinh(t\alpha)\sinh(t\theta)]},$$

$$B_{61}=B_{51},\quad B_{62}=B_{26},\quad B_{63}=B_{53},\quad B_{64}=B_{25},\quad B_{65}=B_{56},\quad B_{66}=B_{55}. \tag{A3}$$

The ultimate relation between the 19 input fields ($\hat{a}_{10}$, $\hat{b}_{10}^{\dagger}$, $\hat{v}_{30}^{\dagger}$, $\hat{b}_{30}^{\dagger}$, $\hat{a}_{20}$, $\hat{a}_{30}$, $\hat{v}_1$, $\hat{v}_2^{\dagger}$, $\hat{v}_3^{\dagger}$, $\hat{v}_4^{\dagger}$, $\hat{v}_5$, $\hat{v}_6$, $\hat{v}_{11}$, $\hat{v}_{21}^{\dagger}$, $\hat{v}_{31}^{\dagger}$, $\hat{v}_{41}^{\dagger}$, $\hat{v}_{51}$, and $\hat{v}_{61}$) and six output fields ($\hat{a}_1$, $\hat{b}_1^{\dagger}$, $\hat{b}_{21}^{\dagger}$, $\hat{b}_3^{\dagger}$, $\hat{a}_2$, and $\hat{a}_3$) in Sec. II is shown as Eq. (7). The coefficient

$$K_c=\frac{\sqrt{\xi}}{\theta+e^{-i\phi}\sqrt{\eta k\zeta_b}[\theta\cosh(t\alpha)\cosh(t\theta)+\beta\sinh(t\alpha)\sinh(t\theta)]}.$$

The detailed matrix element C_{ij} is as follows:

$$C_{11}=\sqrt{\zeta_a}\left\{\frac{\sqrt{\eta k\zeta_b}e^{-i\phi}[\theta^2\cosh^2(\theta t)-\beta^2\sinh^2(\theta t)]}{\theta}+\theta\cosh(\theta t)\cosh(t\alpha)+\beta\sinh(\theta t)\sinh(t\alpha)\right\},$$

$$C_{12}=\frac{\sqrt{\zeta_a}(\beta^2-\theta^2)[-2\sinh(\theta t)\cosh(t\alpha)-\sqrt{\eta k\zeta_b}e^{-i\phi}\sinh(2\theta t)]}{4\varepsilon_1},$$

$$C_{13}=\sqrt{\eta(1-k)\zeta_a}e^{-i\phi}[\theta\cosh(\theta t)\sinh(t\alpha)+\beta\sinh(\theta t)\cosh(t\alpha)],\quad C_{14}=C_{12},$$

$$C_{15}=C_{16}=\frac{\sqrt{\zeta_a}e^{-i\phi}(\beta^2-\theta^2)\sinh(\theta t)[\sqrt{\eta k\zeta_b}\beta\sinh(\theta t)-\theta e^{i\phi}\sinh(t\alpha)]}{2\varepsilon_1\theta},$$

$$C_{17}=\sqrt{1-\zeta_a}\{\sqrt{\eta k\zeta_b}e^{-i\phi}[\theta\cosh(\theta t)\cosh(t\alpha)+\beta\sinh(\theta t)\sinh(t\alpha)]+\theta\},$$

$$C_{18}=0,\quad C_{19}=-C_{13}\frac{\sqrt{(1-\zeta_b)k}}{\sqrt{1-k}},\quad C_{110}=C_{111}=C_{112}=0,$$

$$C_{113}=\frac{\sqrt{1-\xi}}{\sqrt{\xi}}\{\theta+e^{-i\phi}\sqrt{\eta k\zeta_b}[\theta\cosh(t\alpha)\cosh(t\theta)+\beta\sinh(t\alpha)\sinh(t\theta)]\},$$

$$C_{114}=C_{115}=C_{116}=C_{117}=C_{118}=0,\quad C_{119}=C_{13}\frac{\sqrt{1-\eta}}{\sqrt{\eta(1-k)}},$$

$$C_{21}=\varepsilon_1\sqrt{\zeta_b}\sinh(\theta t)[\cosh(t\alpha)+\sqrt{\eta k\zeta_b}e^{-i\phi}\cosh(\theta t)],$$

$$C_{22}=\frac{\sqrt{\zeta_b}}{4}\left\{\begin{array}{c}2[\theta\cosh(\varepsilon_6 t)+\theta\cosh(\theta t)\cosh(t\alpha)-\beta\sinh(\theta t)\sinh(t\alpha)]\\+\sqrt{\eta k\zeta_b}e^{-i\phi}\{2\cosh(\varepsilon_6 t)[\theta\cosh(\theta t)\cosh(t\alpha)+\beta\sinh(\theta t)\sinh(t\alpha)]+\theta\cosh(2\theta t)+\theta\cosh(2t\alpha)\}\end{array}\right\},$$

$$C_{23}=\varepsilon_1\sqrt{\eta(1-k)\zeta_b}e^{-i\phi}\sinh(\theta t)\sinh(t\alpha),$$

$$C_{24}=\frac{\sqrt{\zeta_b}}{4}\left\{\begin{array}{c}-2[\theta\cosh(\varepsilon_6 t)-\theta\cosh(\theta t)\cosh(t\alpha)+\beta\sinh(\theta t)\sinh(t\alpha)]\\+\sqrt{\eta k\zeta_b}e^{-i\phi}\{-2\cosh(\varepsilon_6 t)[\theta\cosh(\theta t)\cosh(t\alpha)+\beta\sinh(\theta t)\sinh(t\alpha)]+\theta\cosh(2\theta t)+\theta\cosh(2t\alpha)\}\end{array}\right\},$$

$$C_{25}=\frac{\sqrt{\zeta_b}}{4}\left\{\begin{array}{c}-2[\theta\sinh(\varepsilon_6 t)-\theta\cosh(\theta t)\sinh(t\alpha)+\beta\sinh(\theta t)\cosh(t\alpha)]-\\\sqrt{\eta k\zeta_b}e^{-i\phi}\{2\theta\sinh(\varepsilon_6 t)\cosh(\theta t)\cosh(t\alpha)+\beta[2\sinh(\varepsilon_6 t)\sinh(\theta t)\sinh(t\alpha)+\sinh(2\theta t)]-\theta\sinh(2t\alpha)\}\end{array}\right\},$$

$$C_{26}=\frac{\sqrt{\zeta_b}}{4}\left\{\begin{array}{c}2[\theta\sinh(\varepsilon_6 t)+\theta\cosh(\theta t)\sinh(t\alpha)-\beta\sinh(\theta t)\cosh(t\alpha)]+\\\sqrt{\eta k\zeta_b}e^{-i\phi}\{2\theta\sinh(\varepsilon_6 t)\cosh(\theta t)\cosh(t\alpha)+\beta[2\sinh(\varepsilon_6 t)\sinh(\theta t)\sinh(t\alpha)-\sinh(2\theta t)]+\theta\sinh(2t\alpha)\}\end{array}\right\},$$

$$C_{27}=0,\quad C_{28}=\sqrt{(1-\zeta_b)}\{\theta+e^{-i\phi}\sqrt{\eta k\zeta_b}[\theta\cosh(t\alpha)\cosh(t\theta)+\beta\sinh(t\alpha)\sinh(t\theta)]\},$$

$$C_{29} = -C_{23}\frac{\sqrt{(1-\zeta_b)k}}{\sqrt{1-k}}, \quad C_{210} = C_{211} = C_{212} = C_{213} = 0,$$

$$C_{214} = C_{113}, \quad C_{215} = C_{216} = C_{217} = C_{218} = 0, \quad C_{219} = C_{23}\frac{\sqrt{1-\eta}}{\sqrt{\eta(1-k)}},$$

$$C_{31} = \sqrt{(1-k)\zeta_b}[\theta\cosh(\theta t)\sinh(t\alpha) + \beta\sinh(\theta t)\cosh(t\alpha)], \quad C_{32} = C_{23}\frac{e^{i\phi}(-\beta^2+\theta^2)}{2\varepsilon_1^2\sqrt{\eta}},$$

$$C_{33} = \theta\sqrt{k} + \sqrt{\eta\zeta_b}e^{-i\phi}[\theta\cosh(\theta t)\cosh(t\alpha) + \beta\sinh(\theta t)\sinh(t\alpha)],$$

$$C_{34} = C_{32}, \quad C_{35} = C_{32}\coth(t\alpha), \quad C_{36} = C_{35}, \quad C_{37} = C_{38} = 0,$$

$$C_{39} = \theta\sqrt{(1-k)(1-\zeta_b)}, \quad C_{310} = C_{311} = C_{312} = C_{313} = C_{314} = 0, \quad C_{315} = C_{113}, \quad C_{316} = C_{317} = C_{318} = 0,$$

$$C_{319} = \sqrt{(1-\eta)(1-k)\zeta_b}e^{-i\phi}[\theta\cosh(\theta t)\cosh(t\alpha) + \beta\sinh(\theta t)\sinh(t\alpha)],$$

$$C_{41} = C_{21}, \quad C_{42} = C_{24}, \quad C_{43} = C_{23}, \quad C_{44} = C_{22}, \quad C_{45} = C_{26}, \quad C_{46} = C_{25}, \quad C_{47} = C_{48} = 0, \quad C_{49} = C_{29}, \quad C_{410} = C_{28},$$

$$C_{411} = C_{412} = C_{413} = C_{414} = C_{415} = 0, \quad C_{416} = C_{113}, \quad C_{417} = C_{418} = 0, \quad C_{419} = C_{219},$$

$$C_{51} = \varepsilon_1\sqrt{\zeta_a}\sinh(\theta t)\left[\sinh(t\alpha) - \frac{\sqrt{\eta k\zeta_b}\beta e^{-i\phi}\sinh(\theta t)}{\theta}\right],$$

$$C_{52} = \frac{\sqrt{\zeta_a}}{2}\left\{\begin{array}{c}-[\theta\sinh(\varepsilon_6 t) - \theta\cosh(\theta t)\sinh(t\alpha) + \beta\sinh(\theta t)\cosh(t\alpha)] - \\ \sqrt{\eta k\zeta_b}e^{-i\phi}\{\theta\cosh(t\alpha)[\sinh(\varepsilon_6 t)\cosh(\theta t) - \sinh(t\alpha)] + \beta\sinh(\theta t)[\sinh(\varepsilon_6 t)\sinh(t\alpha) + \cosh(\theta t)]\}\end{array}\right\},$$

$$C_{53} = C_{23}\frac{\sqrt{\zeta_a}}{\sqrt{\zeta_b}}\coth(t\alpha),$$

$$C_{54} = \frac{\sqrt{\zeta_a}}{4}\left\{\begin{array}{c}2\theta[\sinh(\varepsilon_6 t) + \cosh(\theta t)\sinh(t\alpha)] - 2\beta\sinh(\theta t)\cosh(t\alpha) + \\ \sqrt{\eta k\zeta_b}e^{-i\phi}[2\theta\sinh(\varepsilon_6 t)\cosh(\theta t)\cosh(t\alpha) + 2\beta\sinh(\varepsilon_6 t)\sinh(\theta t)\sinh(t\alpha) + \theta\sinh(2t\alpha) - \beta\sinh(2\theta t)]\end{array}\right\},$$

$$C_{55} = \frac{\sqrt{\zeta_a}}{4\theta}\left\{\begin{array}{c}2\theta^2[\cosh(\varepsilon_6 t) + \cosh(\theta t)\cosh(t\alpha)] - 2\beta\theta\sinh(\theta t)\sinh(t\alpha) + \\ \sqrt{\eta k\zeta_b}e^{-i\phi}\{2\theta\cosh(\varepsilon_6 t)[\theta\cosh(\theta t)\cosh(t\alpha) + \beta\sinh(\theta t)\sinh(t\alpha)] + \theta^2[1+\cosh(2t\alpha)] + \beta^2[\cosh(2\theta t) - 1]\}\end{array}\right\},$$

$$C_{56} = \frac{\sqrt{\zeta_a}}{4\theta}\left\{\begin{array}{c}-2\theta^2[\cosh(\varepsilon_6 t) - \cosh(\theta t)\cosh(t\alpha)] + 2\beta\theta\sinh(\theta t)\sinh(t\alpha) - \\ \sqrt{\eta k\zeta_b}e^{-i\phi}\{2\theta\cosh(\varepsilon_6 t)[\theta\cosh(\theta t)\cosh(t\alpha) + \beta\sinh(\theta t)\sinh(t\alpha)] - \theta^2[1+\cosh(2t\alpha)] - \beta^2[\cosh(2\theta t) - 1]\}\end{array}\right\},$$

$$C_{57} = C_{58} = 0, \quad C_{59} = C_{29}\frac{\sqrt{\zeta_a}}{\sqrt{\zeta_b}}\coth(t\alpha), \quad C_{510} = 0, \quad C_{511} = C_{17}, \quad C_{512} = C_{513} = C_{514} = C_{515} = C_{516} = 0,$$

$$C_{517} = C_{113}, \quad C_{518} = 0, \quad C_{519} = C_{219}\frac{\sqrt{\zeta_a}}{\sqrt{\zeta_a}}\coth(t\alpha),$$

$$C_{61} = C_{51}, \quad C_{62} = C_{54}, \quad C_{63} = C_{53}, \quad C_{64} = C_{52}, \quad C_{65} = C_{56}, \quad C_{66} = C_{55}, \quad C_{67} = C_{68} = 0, \quad C_{69} = C_{59},$$

$$C_{610} = C_{611} = 0, \quad C_{612} = C_{17}, \quad C_{613} = C_{614} = C_{615} = C_{616} = C_{617} = 0, \quad C_{618} = C_{113}, \quad C_{619} = C_{519}, \tag{A4}$$

where α, β, and θ are defined as Eq. (A2).

[1] H. Mabuchi and N. Khaneja, Principles and applications of control in quantum systems, Int J. Robust Nonlin. **15**, 647 (2005).

[2] M. James, Optimal quantum control theory, Annu. Rev. Control Robot. Auton. **4**, 343 (2021).

[3] C. Sayrin, I. Dotsenko, X. Zhou, B. Peaudecerf, T. Rybarczyk, S. Gleyzes, P. Rouchon, M. Mirrahimi, H. Amini, M. Brune, J. M. Raimond, and S. Haroche, Real-time quantum feedback prepares and stabilizes photon number states, Nature (London) **477**, 73 (2011).

[4] N. Yamamoto, Coherent versus measurement feedback: Linear systems theory for quantum information, Phys. Rev. X **4**, 041029 (2014).

[5] M. Ernzer, M. Bosch Aguilera, M. Brunelli, G.-L. Schmid, T. M. Karg, C. Bruder, P. P. Potts, and P. Treutlein, Optical coherent feedback control of a mechanical oscillator, Phys. Rev. X **13**, 021023 (2023).

[6] Y. Han, Z. Zhang, J. Qu, and W. Diao, Entanglement enhancement from coherent feedback-controlled and cascaded nondegenerate optical parametric amplifiers, Opt. Commun. **526**, 128858 (2023).

[7] S. Borah, B. Sarma, M. Kewming, G. J. Milburn, and J. Twamley, Measurement-based feedback quantum control with deep reinforcement learning for a double-well nonlinear potential, Phys. Rev. Lett. **127**, 190403 (2021).

[8] L. Qiu, G. Huang, I. Shomroni, J. Pan, P. Seidler, and T. J. Kippenberg, Dissipative quantum feedback in measurements using a parametrically coupled microcavity, PRX Quantum **3**, 020309 (2022).

[9] J. Zhang, Y. Liu, R. Wu, K. Jacobs, and F. Nori, Quantum feedback: Theory, experiments, and applications, Phys. Rep. **679**, 1 (2017).

[10] J. E. Gough and S. Wildfeuer, Enhancement of field squeezing using coherent feedback, Phys. Rev. A **80**, 042107 (2009).

[11] S. Iida, M. Yukawa, H. Yonezawa, N. Yamamoto, and A. Furusawa, Experimental demonstration of coherent feedback control on optical field squeezing, IEEE Trans. Autom. Control. **57**, 2045 (2012).

[12] M. Yanagisawa and H. Kimura, Transfer function approach to quantum control-part I: Dynamics of quantum feedback systems, IEEE Trans. Autom. Control. **48**, 2107 (2003).

[13] Z. Yan, X. Jia, C. Xie, and K. Peng, Coherent feedback control of multipartite quantum entanglement for optical fields, Phys. Rev. A **84**, 062304 (2011).

[14] K. Jacobs, X. Wang, and H. M. Wiseman, Coherent feedback that beats all measurement-based feedback protocols, New J. Phys. **16**, 073036 (2014).

[15] B. Qi and L. Guo, Is measurement-based feedback still better for quantum control systems? Syst. Control Lett. **59**, 333 (2010).

[16] J. Kerckhoff, H. I. Nurdin, D. S. Pavlichin, and H. Mabuchi, Designing quantum memories with embedded control: Photonic circuits for autonomous quantum error correction, Phys. Rev. Lett. **105**, 040502 (2010).

[17] J. Kerckhoff, D. S. Pavlichin, H. Chalabi, and H. Mabuchi, Design of nanophotonic circuits for autonomous subsystem quantum error correction, New J. Phys. **13**, 055022 (2011).

[18] S. Qin, X. Xin, S. He, and C. Li, Enhancement of quantum correlations in a cavity–magnon system with feedback control, J. Opt. Soc. Am. B **38**, 3902 (2021).

[19] M. Amazioug, B. Teklu, and M. Asjad, Enhancement of magnon-photon-phonon entanglement in a cavity magnomechanics with coherent feedback loop, Sci. Rep. **13**, 3833 (2023).

[20] S. L. Braunstein and P. van Loock, Quantum information with continuous variables, Rev. Mod. Phys. **77**, 513 (2005).

[21] H. Kimble, The quantum internet, Nature (London) **453**, 1023 (2008).

[22] K. Zhang, S. Liu, Y. Chen, X. Wang, and J. Jing, Optical quantum states based on hot atomic ensembles and their applications, Photon. Insights **1**, R06 (2022).

[23] X. Pan, H. Chen, T. Wei, J. Zhang, A. M. Marino, N. Treps, R. T. Glasser, and J. Jing, Experimental realization of a feedback optical parametric amplifier with four-wave mixing, Phys. Rev. B **97**, 161115(R) (2018).

[24] Y. Zhong and J. Jing, Enhancement of tripartite quantum correlation by coherent feedback control, Phys. Rev. A **101**, 023813 (2020).

[25] H. Wang, C. Fabre, and J. Jing, Single-step fabrication of scalable multimode quantum resources using four-wave mixing with a spatially structured pump, Phys. Rev. A **95**, 051802(R) (2017).

[26] K. Zhang, W. Wang, S. Liu, X. Pan, J. Du, Y. Lou, S. Yu, S. Lv, N. Treps, C. Fabre, and J. Jing, Reconfigurable hexapartite entanglement by spatially multiplexed four-wave mixing processes, Phys. Rev. Lett. **124**, 090501 (2020).

[27] H. Wang, K. Zhang, N. Treps, C. Fabre, J. Zhang, and J. Jing, Generation of hexapartite entanglement in a four-wave-mixing process with a spatially structured pump: Theoretical study, Phys. Rev. A **102**, 022417 (2020).

[28] P. van Loock and A. Furusawa, Detecting genuine multipartite continuous-variable entanglement, Phys. Rev. A **67**, 052315 (2003).

[29] R. F. Werner and M. M. Wolf, Bound entangled Gaussian states, Phys. Rev. Lett. **86**, 3658 (2001).

[30] R. Simon, Peres-Horodecki separability criterion for continuous variable systems, Phys. Rev. Lett. **84**, 2726 (2000).

[31] K. N. Cassemiro and A. S. Villar, Scalable continuous-variable entanglement of light beams produced by optical parametric oscillators, Phys. Rev. A **77**, 022311 (2008).

[32] Y. Liang, R. Yang, J. Zhang, and T. Zhang, Hexapartite steering based on a four-wave-mixing process with a spatially structured pump, Opt. Express **31**, 11775 (2023).

[33] K. Zhang, Y. Guo, and J. Jing, Reconfigurable hexapartite cluster states by four-wave mixing processes with a spatially structured pump, Adv. Quantum Technol. **7**, 2300160 (2024).

[34] M. Jasperse, L. Turner, and R. Scholten, Relative intensity squeezing by four-wave mixing with loss: An analytic model and experimental diagnostic, Opt. Express **19**, 3765 (2011).

[35] H. He, S. Liu, Y. Lou, and J. Jing, Characterization of quantum squeezing generated from the phase-sensitive and phase-insensitive amplifiers in the ultra-low average input photon number regime, Opt. Express **28**, 36487 (2020).

[36] S. Liu, Y. Lou, and J. Jing, Interference-induced quantum squeezing enhancement in a two-beam phase-sensitive amplifier, Phys. Rev. Lett. **123**, 113602 (2019).

[37] G. Vidal and R. F. Werner, Computable measure of entanglement, Phys. Rev. A **65**, 032314 (2002).

[38] J. Aasi, J. Abadie, B. Abbott, R. Abbott, T. Abbott, M. Abernathy, C. Adams, T. Adams, P. Addesso, R. Adhikari *et al.*, Enhanced sensitivity of the ligo gravitational wave detector by using squeezed states of light, Nat. Photon. **7**, 613 (2013).